Effect of helium-ion implantation on 3*C*-SiC nanomechanical string resonators

Philipp Bredol,[1,*] Felix David,[1] Nagesh S. Jagtap,[2,3] Yannick S. Klaß,[1] Georgy V. Astakhov,[2,†] Artur Erbe,[2,4,‡] and Eva M. Weig[1,5,6,§]

[1] *Department of Electrical Engineering, School of Computation, Information and Technology, Technical University of Munich, 85748 Garching, Germany*
[2] *Institute of Ion Beam Physics and Materials Research, Helmholtz-Zentrum Dresden-Rossendorf, 01328 Dresden, Germany*
[3] *Faculty of Physics, TU Dresden, 01069 Dresden, Germany*
[4] *Faculty of Electrical and Computer Engineering, TU Dresden, 01069 Dresden, Germany*
[5] *Munich Center for Quantum Science and Technology, 80799 Munich, Germany*
[6] *TUM Center for Quantum Engineering (ZQE), 85748 Garching, Germany*

(Received 21 June 2024; revised 8 August 2024; accepted 13 August 2024; published 13 September 2024)

Hybrid quantum devices enable novel functionalities by combining the benefits of different subsystems. Particularly, point defects in nanomechanical resonators made of diamond or silicon carbide (SiC) have been proposed for precise magnetic field sensing and as versatile quantum transducers. However, the realization of a hybrid system may involve trade-offs in the performance of the constituent subsystems. In a spin-mechanical system, the mechanical properties of the resonator may suffer from the presence of engineered defects in the crystal lattice. This may severely restrict the performance of the resulting device and needs to be carefully explored. Here we focus on the impact of defects on high-Q nanomechanical string resonators made of prestressed 3C-SiC grown on Si(111). We use helium-ion implantation to create point defects and study their accumulated effect on the mechanical performance. Using Euler-Bernoulli beam theory, we present a method to determine Young's modulus and the prestress of the strings. We find that Young's modulus is not modified by implantation. Under implantation doses relevant for single-defect or defect-ensemble generation, both tensile stress and damping rate also remain unaltered. For a higher implantation dose, both exhibit a characteristic change.

DOI: 10.1103/PhysRevApplied.22.034036

I. INTRODUCTION

Using quantum phenomena such as coherence, superposition, interference, and entanglement, today's quantum technology can create, manipulate, and detect single photons, phonons, and spins [1,2]. Hybrid quantum devices combine different subsystems to go beyond the limitations that their components face in stand-alone applications and have been theoretically and experimentally investigated [3,4]. Current nanofabrication techniques enable the coupling of mechanical resonators to electromagnetic radiation by integrating mechanical resonators in optical cavities and superconducting microwave circuits, making cavity optomechanical systems [5] a potential candidate for future quantum technologies. Further, hybrid spin-mechanical systems enable the coupling of phonons from the mechanical mode of a membrane or cantilever to the spin, for example, of a point defect. Hybrid spin-mechanical systems with diamond using nitrogen-vacancy centers have been studied [4,6]. However, challenges persist in the growth, fabrication, and device processing of diamond [7].

On the other hand, SiC is a technologically and industrially established material in the field of power electronics. More importantly, several polytypes of SiC have gained importance as a material for nanoelectromechanical systems [8–15]. Also, SiC hosts point defects with highly coherent spin degrees of freedom, such as the silicon vacancy (V_{Si}) [16,17] and the divacancy [18]. Such point defects can be created efficiently by ion-implantation techniques with nanometer precision [19,20].

Our long-term goal is to realize a hybrid spin-mechanical system to improve magnetic field sensing—for example, based on spins associated with V_{Si} in a nanomechanical resonator made of 4H-SiC [21]. To obtain a thorough understanding of the impact of defect generation on the mechanical performance, we use nanoresonators fabricated in 3C-SiC grown on Si [8–11]. This material platform provides well-established and reliable process

*Contact author: philipp.bredol@tum.de
†Contact author: g.astakhov@hzdr.de
‡Contact author: a.erbe@hzdr.de
§Contact author: eva.weig@tum.de

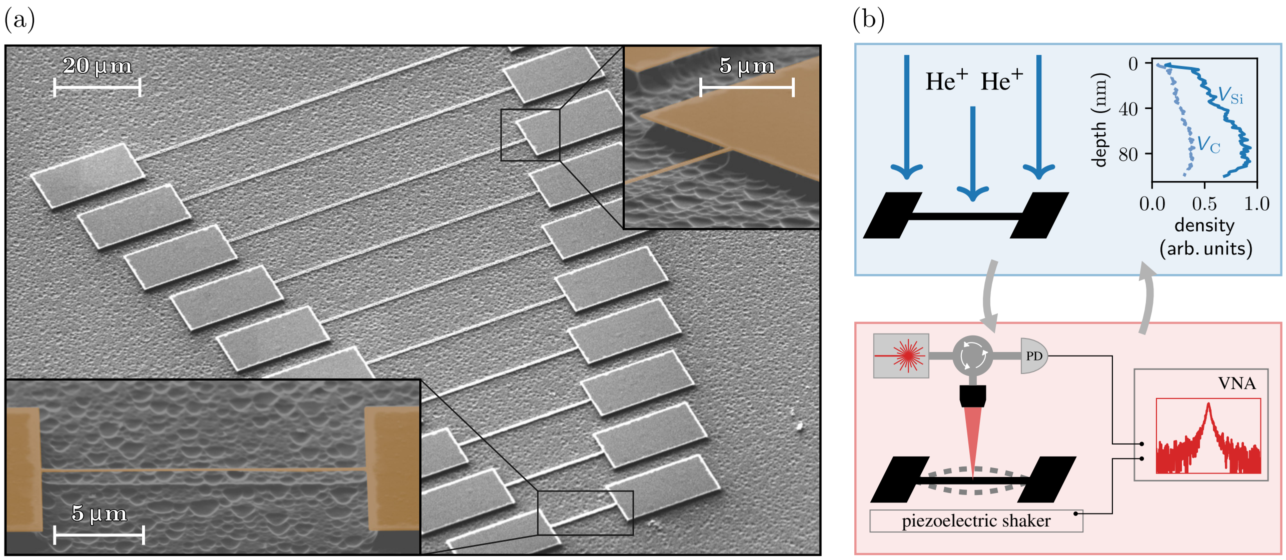

FIG. 1. (a) Scanning electron micrograph of an array of string resonators with lengths between 20 and 110µm. The insets show false-color tilted-view close-ups of individual strings. Strings and clamping pads are highlighted in orange; the "shadow" underneath results from underetching. (b) Consecutive-measurement procedure alternating between He-ion implantation (top) and nanomechanical characterization (bottom). Characterization is performed by means of piezoelectric actuation and optical interferometric detection via a fast photodetector (PD) with a vector network analyzer (VNA). For further details, see Appendix C. The upper-right inset shows simulated depth profiles of the normalized density of silicon vacancies and carbon vacancies created by the implantation.

routines for freely suspended nanostructures. In addition, 3*C*-SiC grown on Si(111) features a strong tensile prestress owing to a 20% lattice mismatch [22]. Prestress may increase the mechanical quality factor by orders of magnitude due to dissipation dilution [23–25], which was first reported in amorphous-SiN nanomechanical resonators [26] and later extended to crystalline (In,Ga)P [27], Si [28], AlN [29], SiC [12–14], and amorphous SiC [30]. Thus, prestressed 3*C*-SiC nanomechanical string resonators serve as an ideal platform for detecting small changes in mechanical properties with high precision, while our findings can be qualitatively applied to other polytypes of SiC.

To systematically evaluate trends in the mechanical performance, we chose an iterative approach that allows us to increase the defect concentration in the resonators under investigation. We start by fabricating nanomechanical string resonators and carefully characterize their vibrational properties. A comprehensive eigenmode analysis is performed to extract all nanomechanical figures of merit—namely, the tensile stress σ, Young's modulus E, and damping rate Γ of the individual nanoresonators. Subsequently, we apply broad-beam He-ion implantation (Fig. 1) to create defects in the nanostring resonators and repeat the mechanical characterization. This procedure is repeated, starting from a low ion fluence with continuously increasing fluence until clear damage of the nanostring resonators is observed. Helium is chosen due to its narrow interaction volume of a few $(100\ \mathrm{nm})^3$ and minimal spread of defect formation [31,32]. This results in the generation of ensembles of silicon vacancies and carbon vacancies (V_C), as well as further, less-important defects.

Previous research on the effect of implantation-induced defects on the mechanical properties was done in the context of nuclear-reactor materials and covers the huge fluences that nuclear-reactor walls have to withstand [33–36]. However, little is known about the low fluences that are applied to create defects for quantum technologies. Our work fills this gap by reporting the effect of helium-ion implantation in the low-damage regime on the properties of high-Q nanomechanical resonators.

II. METHODS

A. Fabrication of prestressed nanomechanical string resonators

Nanomechanical resonators are fabricated from a 110-nm 3*C*-SiC(111) thin film that has been epitaxially grown on a Si(111) wafer by NovaSIC. We use electron-beam lithography and a combination of dry-etching techniques to realize arrays of freely suspended nanostrings, i.e., one-dimensional doubly clamped mechanical resonators, of different lengths as shown in Fig. 1. The geometric parameters of the fabricated strings are listed in Table I.

Importantly, the resonators fabricated feature a strong tensile prestress inherited from the thin-film wafer. This

TABLE I. Material and sample parameters and their uncertainties used for the fits to Euler-Bernoulli beam theory [Eq. (1)]. l_0 denotes the nominal length of the lithography design. The parameters shown apply to all the devices discussed in this work.

String thickness	$h = 110(2)$ nm	Ref. [14]
String width	$w = 360(30)$ nm	
String length	$l = l_0 \pm 500$ nm	Ref. [14]
with	$l_0 = 20$–$110\ \mu$m	
Mass density	$\rho = 3.2(1) \times 10^3$ kg m^{-3}	Refs. [37,38]

static prestress is created during the epitaxial-growth process because of the large mismatch of lattice constants (20%) and thermal-expansion coefficients (8%) of the 3C-SiC film and the Si substrate [22]. During the further processing steps, this strong prestress may relax or increase depending on the device geometry [39]. For the nanostring geometry discussed here, the prestress after fabrication is uniaxial and lies between 0.75 and 0.85 GPa. We determine the resulting tensile prestress of our string resonators, along with the other mechanical figures of merit, by analyzing the mechanical response spectra, as described at the end of this section. For further details, see Appendix A.

B. He-ion implantation

Controlled generation of ensembles of silicon vacancies in the precharacterized nanostring resonators is accomplished by He broad-beam ion implantation with a DANFYS 1090-50 implanter (see Appendix B). We choose an implantation energy of 14 keV, which corresponds to a projected range of 95 nm. Figure 1(b) depicts the normalized densities of created silicon and carbon vacancies as a function of depth found by a STOPPING AND RANGE OF IONS IN MATTER (SRIM) simulation.

The samples are consecutively exposed to He fluences between 10^{12} and 10^{14} cm^{-2}. According to the SRIM simulation, a fluence of 10^{14} cm^{-2} creates approximately 4×10^{20} $V_{\mathrm{Si}}/\mathrm{cm}^2$ and approximately 2×10^{20} $V_{\mathrm{C}}/\mathrm{cm}^2$. The actual defect densities obtained are lower because a large number of the created defects immediately anneal again at room temperature [36,40].

C. Measurement of mechanical-response spectra

To characterize the nanoresonators, we obtain frequency-response spectra of a large number of harmonic eigenmodes of all nanostrings. To this end, the drive frequency applied to a piezoelectric shaker underneath the sample is swept across all resonances, and the mechanical response at the drive frequency is read out by means of optical interferometry [Fig. 1(b)] [41]. The sample and piezoelectric shaker are mounted on an x-y-z positioner stage to address individual string resonators. To eliminate the effect of gas damping, the measurements are done at pressures below 10^{-3} mbar. See Appendix C for a detailed description of the measurement setup.

The linear frequency response of the fundamental out-of-plane mode of an exemplary string with $l = 100\ \mu$m is displayed in Fig. 2(a) for a range of implantation fluences. The upper-left inset in Fig. 2(c) shows these frequencies plotted against the accumulated fluence. To ensure that the linewidth of the response curve is not broadened by spectral diffusion, we spot-check compatibility with ringdown measurements [Fig. 2(b)].

D. Euler-Bernoulli-beam-theory fits

The recorded frequency-response curves are fit to Eq. (D2) to determine the resonance frequency and damping rate, as illustrated in Fig. 2(a) (see Appendix D for details). Furthermore, we deduce the tensile stress σ and the Young's modulus E by fitting the resonance frequencies before and after each implantation step to the expected frequencies of an Euler-Bernoulli beam with simply supported boundary conditions:

$$f(n) = \frac{n^2\pi}{2l^2}\sqrt{\frac{Eh^2}{12\rho}}\sqrt{1 + \frac{12\sigma l^2}{n^2\pi^2 Eh^2}}, \qquad (1)$$

with mode number n, string length l, material mass density ρ, Young's modulus E, tensile prestress σ, and string thickness h measured along the oscillation direction. Equation (1) holds if $l/h \gg 1$ and $w/h < 5$ [42], which all the devices discussed fulfill (Table I). The quantities σ and E are free fit parameters, and l, ρ, and h are taken from Table I. We find that the measured frequencies and the fit function are in agreement [Fig. 2(c)], thereby justifying the choice of boundary conditions for our devices.

We estimate the uncertainties of the optimal-fit-parameter results using Monte Carlo error propagation. For that purpose, each frequency is remeasured multiple times during the characterization. For each Monte Carlo run, one of these measured frequencies is picked at random for each mode. l, ρ, and h are drawn from a normal distribution for each run, with the standard deviation given by the respective parameter uncertainty (Table I). We run the fit for many of these random choices of parameters and frequencies. The uncertainties of σ and E are then given by the standard deviation of the fit results of all runs. This error-propagation method is closely related to the method presented in Ref. [14] but is more forgiving with respect to outlier frequencies, which helps us in analyzing the large datasets generated in this work.

Inserting the material parameters of our samples in Eq. (1), one finds that the frequencies are given by $f(n) \overset{\propto}{\sim} \sqrt{\sigma} n$, i.e., the stress is related to the slope of $f(n)$, which can be fit reliably even with few data points. The Young's modulus E, however, corresponds to a tiny nonlinear component of $f(n)$, which accounts for the contribution of the bending rigidity to the string's dynamics and becomes apparent only for higher modes [Fig. 2(c)].

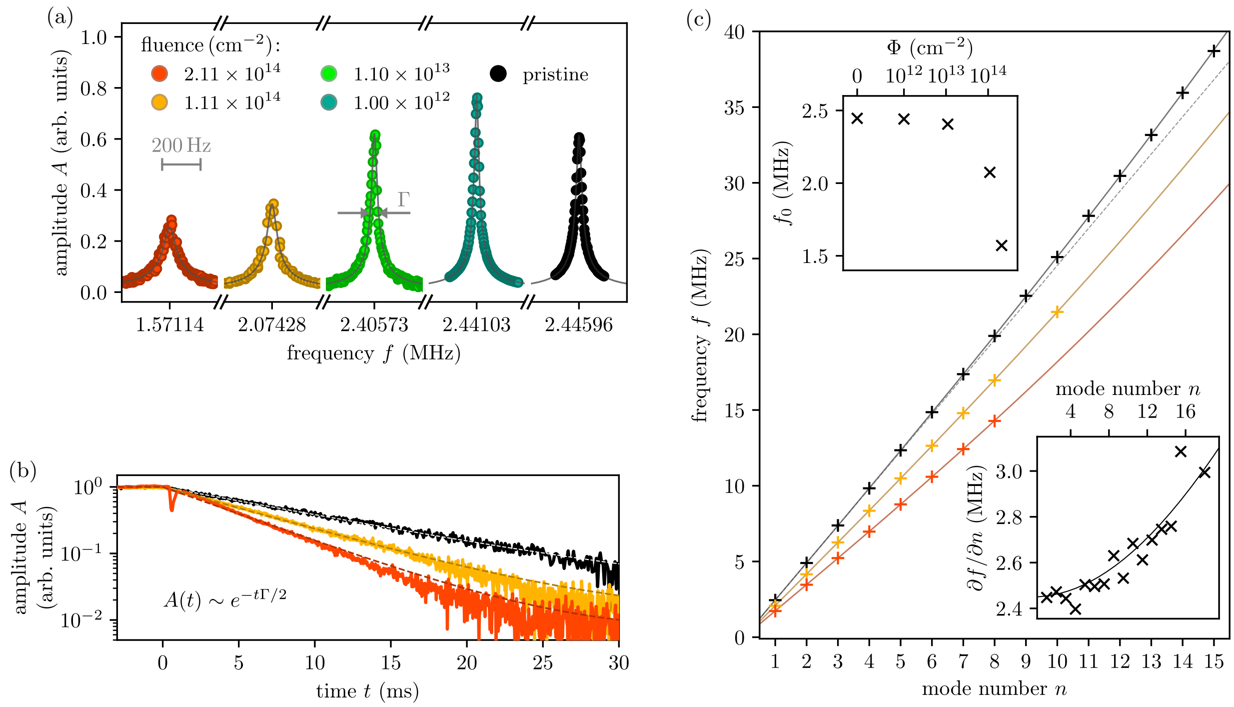

FIG. 2. (a) Measured resonance curves (dots) and fits (solid lines) of the fundamental mode of a string with $l = 100$ µm (further parameters are given in Table I) on sample A after being subjected to multiple ion-irradiation iterations with increasing fluence. The damping rates Γ obtained from the linewidths are 408, 290, 166, 132, and 163 Hz, respectively (left to right). All peaks are normalized to enclose the same area $\int A\, df$. (b) Corresponding ringdown measurements of the same string for three different fluences (color code). The damping rates Γ obtained by fitting an exponential decay curve (dashed lines) are 378, 297, and 199 Hz (bottom to top), agreeing with the damping rates determined from the response-curve fits. See Appendix D for the fit functions and conventions used. (c) Resonance frequencies (crosses) of the same string as a function of mode number for three different fluences (color code) and fits to Eq. (1) (lines). The dashed line follows the linear $f(n) = nf_0$ scaling law. The lower-right inset shows the derivative of the resonance frequency with respect to the mode number for the pristine data and fit. The dashed line and the lower-right inset highlight the small nonlinear component of the measured curves accounting for the bending contribution, which encodes the material's Young's modulus. The upper-left inset shows the resonance frequencies from (a) as a function of accumulated fluence.

This leads to E being more sensitive to the uncertainties of measured frequencies, geometry, and material parameters than the fit parameter σ. Thus, the results for the Young's modulus E tend to show larger relative uncertainties than the results for the stress σ.

III. RESULTS AND DISCUSSION

Two samples were fabricated and are referred to as "sample A" and "sample B." All visible mechanical modes of 14 different strings were characterized on sample A for the pristine state and at four different ion fluences. To evaluate the sample-to-sample variation of the observed trends, we additionally characterized 15 strings on sample B at two different fluences. The shift of the fundamental-mode frequency and the resonance broadening is clearly observed with increasing He implantation fluence Φ [Fig. 2(a)].

A. Ion-induced stress relaxation

Figure 3 shows the stress obtained from the Euler-Bernoulli beam fits [Eq. (1)] for all fluences

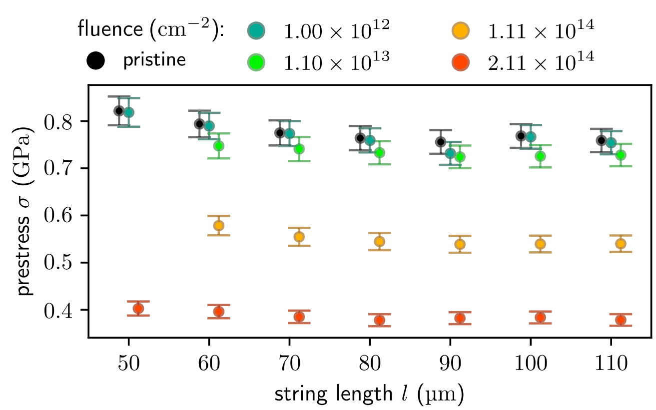

FIG. 3. Tensile prestress extracted from each string's frequency response (see Fig. 2) as a function of string length for sample A. The color indicates the accumulated fluence, the error bars show the combined uncertainty of the included geometry parameters, material parameters, and fit uncertainty. Data are slightly x-shifted for clarity.

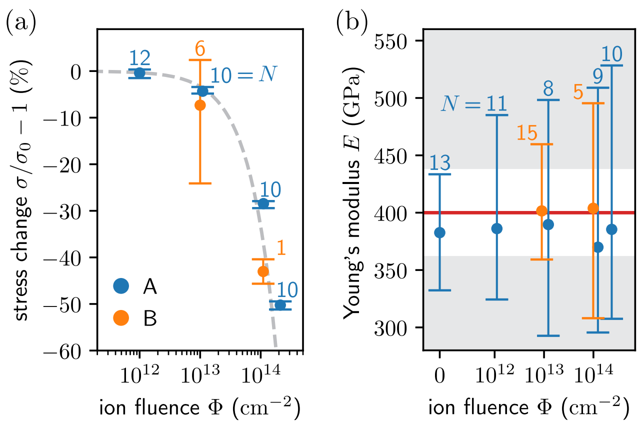

FIG. 4. (a) Tensile prestress σ as a function of accumulated fluence Φ normalized to the initial prestress σ_0 of the pristine string resonator averaged over string length for samples A (blue) and B (orange). The error bars indicate the standard deviation. The numbers close to the error bars indicate the number of underlying data points. The dashed line traces the relation $\sigma/\sigma_0 = 1 - \Phi/\Phi_{0,\sigma}$ with $\Phi_{0,\sigma} = 3 \times 10^{14}\,\mathrm{cm}^{-2}$. (b) Equivalent plot of Young's modulus. The red line and the shaded region indicate $E = 400(38)$ GPa as determined in Ref. [14].

investigated. For the pristine sample, the prestress increases with shortening string length, which is a side effect of stress redistribution during etching [39]. After the initial $\Phi = 10^{12}\,\mathrm{cm}^{-2}$ implantation, the prestress is still close to the prestress of the pristine string, indicating a negligible shift of mechanical eigenfrequencies up to this fluence. During the further implantation runs, the stress significantly relaxes [Fig. 4(a)]. The dependence of this stress relaxation on the fluence follows the simple phenomenological relation

$$\frac{\sigma(\Phi)}{\sigma_0} = 1 - \frac{\Phi}{\Phi_{0,\sigma}}, \tag{2}$$

with Φ denoting the total He-ion fluence that the sample was exposed to, $\sigma(\Phi)$ denoting the remaining prestress at a given fluence, σ_0 denoting the prestress of the pristine sample, and $\Phi_{0,\sigma}$ denoting a phenomenological parameter that corresponds to the fluence at which the prestress would be fully relaxed ($3 \times 10^{14}\mathrm{cm}^{-2}$ for our samples). This relation is compatible with volumetric material swelling in proportion to the implanted-He-ion fluence, which agrees with previous measurements [35] and simulations [33].

B. Independence of Young's modulus

Whereas we observe a significant relaxation of the prestress, Young's modulus stays constant within the error margins for both samples and all fluences used [Fig. 4(b)]. This observation agrees with the findings of previous experiments determining the Young's modulus of SiC by nanoindentation [34,43] and molecular-dynamics simulations [33]. The uncertainties of the extracted values for Young's modulus tend to increase with the accumulated ion fluence because fewer mechanical modes were visible the more the sample was transferred between laboratories and setups during the consecutive measurement protocol.

The number of data points used to calculate the standard deviation in the two plots shown in Fig. 4 differs even though the same dataset was used for both plots. On the one hand, obtaining a meaningful E requires a large number of measurable mechanical modes, whereas σ can be determined with only a few modes. On the other hand σ/σ_0 requires the stress of the implanted state and the pristine state to be known.

It is important to note that the Young's modulus values we measure are based on the bending rigidity of the nanostring resonators. This implicitly assumes a slender string with rectangular cross section made from a material with homogeneous elastic properties. These assumptions are perfectly justified for the pristine data. After implantation, however, the latter assumption is not obviously fulfilled. We expect stronger material modification close to the substrate-facing surface of the nanostring resonators than in the rest of the material, due to the implantation profile chosen [Fig. 1(b)]. The fact that we observe no significant change in Young's modulus for the fluence range investigated indicates that the material modifications caused negligible changes in the elastic properties; hence, the assumption of homogeneous elastic properties is also justified after implantation, allowing us to safely deduce Young's modulus from the bending rigidity.

C. Ion-induced mechanical damping

Apart from prestress and Young's modulus, we study the mechanical damping rates of the nanostring resonators as a function of accumulated fluence. The damping rates shown here are obtained from the linewidth fits [Eq. (D2)] of the response curves [Fig. 2(a)]. We spot-check the consistency of the damping rates obtained with ringdown measurements [Fig. 2(b)], to ensure that the measured linewidths reflect the mechanical damping rates and are not broadened by spectral diffusion, instrumentation noise, resolution limits, etc.

Figure 5 shows that the damping rates stay constant within experimental errors up to an accumulated fluence of approximately $10^{13}\,\mathrm{cm}^{-2}$. For higher fluences, however, the damping increases rapidly, indicating that the internal friction caused by the irradiation damage outweighs the other friction mechanisms.

The damping rate of nanostring resonators is sensitive to contamination or other forms of degradation that may occur during mounting, unmounting, and transporting

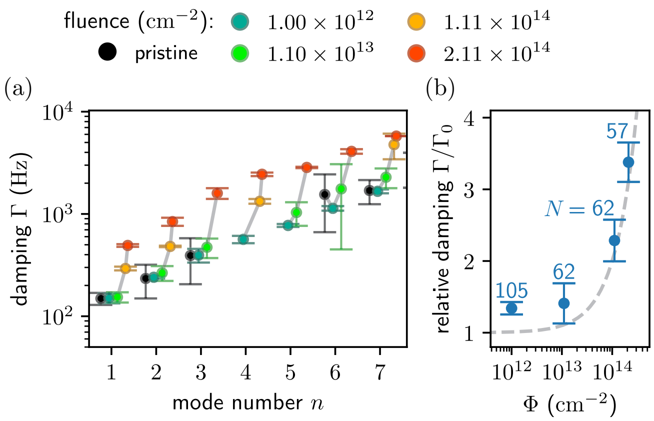

FIG. 5. (a) Dependence of the mechanical damping rate Γ on the accumulated fluence Φ for the first seven flexural out-of-plane modes of an exemplary string with $l = 100\,\mu$m. (b) Damping Γ relative to the respective pristine Γ_0 as a function of Φ averaged over all string lengths and mode numbers measured on sample A. The error bars indicate the standard deviation. The numbers close to the error bars indicate the number of underlying measured values of Γ. The dashed line traces the relation $\Gamma/\Gamma_0 = 1 + \Phi/\Phi_{0,\Gamma}$ with $\Phi_{0,\Gamma} = 10^{14}$ cm^{-2}.

of the sample between the different setups. This limits the repeatability of the damping-rate measurement to $\pm30\%$ in our experiment. The error bars in Fig. 5(b) reflect the standard deviations of measurements done in one run and do not take the repeatability into account. It is worth noting that the two data points in Fig. 5(b) with $\Phi \leq 1.1 \times 10^{13}$ cm^{-2} seem to disagree with the trend indicated by the dashed line. However, considering the repeatability of $\pm30\%$, both points are in good agreement with the trend.

Similarly to the behavior of the string prestress, the relative damping rate Γ/Γ_0 depends linearly on the accumulated fluence [dashed line in Fig. 5(b)]:

$$\frac{\Gamma(\Phi)}{\Gamma_0} = 1 + \frac{\Phi}{\Phi_{0,\Gamma}}, \tag{3}$$

with Φ denoting the accumulated fluence, $\Gamma(\Phi)$ denoting the damping at a given fluence, Γ_0 denoting the corresponding damping in the pristine state, and $\Phi_{0,\Gamma}$ denoting the phenomenological parameter. The slope of this trend is given by $\Phi_{0,\Gamma} = 10^{14}$ cm^{-2} for the ion-induced damping increase and by $\Phi_{0,\sigma} = 3 \times 10^{14}$ cm^{-2} for the stress relaxation. It is known that the various possible point defects contribute differently to the volumetric swelling of SiC [33]. Similarly, their contribution to the inner mechanical friction likely varies too, explaining the different scaling of stress relaxation and damping increase with accumulated fluence.

The optimum implantation fluence to create the V_{Si} ensembles is on the order of 5×10^{13}–10^{14} cm^{-2} [44]. We observe a moderate increase of Γ for this fluence regime. Thus, for hybrid spin-mechanical devices based on defect ensembles, additional mechanical damping caused by the implantation is to be expected. However, the typical implantation fluences required to create isolated optically active silicon vacancies are on the order of 10^{11} cm^{-2} [45]. This fluence is far below the observed threshold of approximately 10^{13} cm^{-2}, at which additional mechanical damping starts to become noticeable. Therefore, for applications based on single defects, additional ion-induced damping is expected to not play a dominant role.

IV. CONCLUSION

We present measurements of the eigenfrequency and damping rates of the flexural out-of-plane modes of nanomechanical string resonators made of strongly prestressed 3*C*-SiC as a function of accumulated helium-ion fluence Φ under broad-beam ion implantation. We obtain the uniaxial tensile prestress and Young's modulus by fitting the measured eigenfrequencies to Euler-Bernoulli beam theory. The method presented can also be applied to other types of mechanical nanodevices, such as cantilevers and membranes.

We find that the prestress relaxes for $\Phi > 10^{13}$ cm^{-2} and drops to 50% of the original value for the highest fluence investigated, $\Phi = 2.11 \times 10^{14}$ cm^{-2}. The stress relaxation agrees with the well-known volumetric swelling of SiC upon helium implantation. Young's modulus remains unchanged for all implantation fluences investigated.

The damping rate stays constant up to a threshold of $\Phi \approx 10^{13}$ cm^{-2} and increases rapidly for higher fluences. We conclude that creating point-defect ensembles for hybrid spin-mechanical devices using ion implantation does not cause excessive additional mechanical damping. When single defects are created, the additional mechanical damping is negligible.

The observed stress relaxation shows that the resonance frequencies of prestressed string resonators are widely tunable by means of He-ion implantation without additional damping being caused, which could be used to individually tune resonators by local implantation in a helium-ion microscope. Usually, the resonance frequencies of two nominally identical prestressed string resonators differ by hundreds of linewidths. Individual tuning in a helium-ion microscope would allow one to fabricate resonators with resonance frequencies matched better than their linewidths or with well-defined frequency splittings to engineer resonant couplings between strings.

The data that support the findings of this study are openly available in Ref. [46].

ACKNOWLEDGMENTS

We gratefully acknowledge financial support from the Deutsche Forschungsgemeinschaft () through Projects No.

AS 310/9-1, No. ER 341/17-1, and No. WE 4721/1-1. Support from the Ion Beam Center and the Nanofabrication Facilities Rossendorf at Ion Beam Center of Helmholtz-Zentrum Dresden-Rossendorf is gratefully acknowledged for ion implantation and nanofabrication. Support from the Center for Nanotechnology and Nanomaterials (ZNN) Garching is gratefully acknowledged for nanofabrication.

APPENDIX A: FABRICATION OF NANOMECHANICAL STRING RESONATORS

We fabricate prestressed nanomechanical string resonators from commercially available 3*C*-SiC thin-film wafers grown on Si(111) by NovaSiC. The nominal 3*C*-SiC film thickness is 110 nm. We pattern four arrays of nanostring resonators as shown in Fig. 1(a) on a $5 \times 5\ \mathrm{mm}^2$ sample using electron-beam lithography and polymethyl methacrylate resist. Each array consists of ten nanostring resonators with lengths increasing from 20 to 110 µm in steps of 10µm [Fig. 1(a) and Table I]. We evaporate 30 nm of Cr followed by a lift-off to obtain the patterned hard mask. Anisotropic reactive-ion etching with SF_6 (2 sccm) and argon (4 sccm) at an inductively-coupled-plasma power of 200 W and radio frequency power of 20 W transfers the pattern into the SiC thin film. We apply isotropic reactive-ion-etching to the silicon substrate to release the strings. Therefore, we also use a gas mixture of SF_6 (30 sccm) and argon (5 sccm) with radio frequency power of 20 W and no inductively-coupled-plasma power. We assume a total etching depth of 1.8 µm. Finally, the Cr hard mask is removed with chromium etchant 1020 from Transene.

APPENDIX B: DANFYS 1090-50 ION IMPLANTER

The implantation machine used is a DANFYS 1090-50 electrostatic air-insulated accelerator produced by Danfysik. The SO140 ion source is integrated directly into the high-voltage terminal. The positively charged ions generated by electron-impact ionization in the ion source are accelerated toward the ion beam line. The maximum acceleration voltage that can be achieved is 40 kV. The sample is scanned with the ion beam in horizontal and vertical directions by deflection of plates supplied with a triangle voltage (frequency around 1 kHz) to achieve homogeneous implantation. The pressure inside the sample chamber is around 1×10^{-7} mbar.

APPENDIX C: CHARACTERIZATION SETUP

Figure 6 shows a sketch of the interferometric measurement setup. Laser light of 1550 nm is sent through half-wave and quarter-wave plates to ensure well-defined linear polarization, which is fully transmitted by the polarizing-beam-splitter cube. The transmitted light is converted to circular polarization by another quarter wave plate and focused on the sample using a standard microscope objective. Since the cross section of the laser spot is larger than the string's width, only part of the light is reflected by the string surface, and the rest is reflected by the silicon substrate (see Sec. 4.2 in Ref. [41]). Because of the interference of these reflections, vibrations of the string modulate the intensity of the reflected light. The reflected light is collected by the objective and converted by the quarter-wave plate back to linearly polarized light, which is fully reflected to the fast photodetector by the PBS.

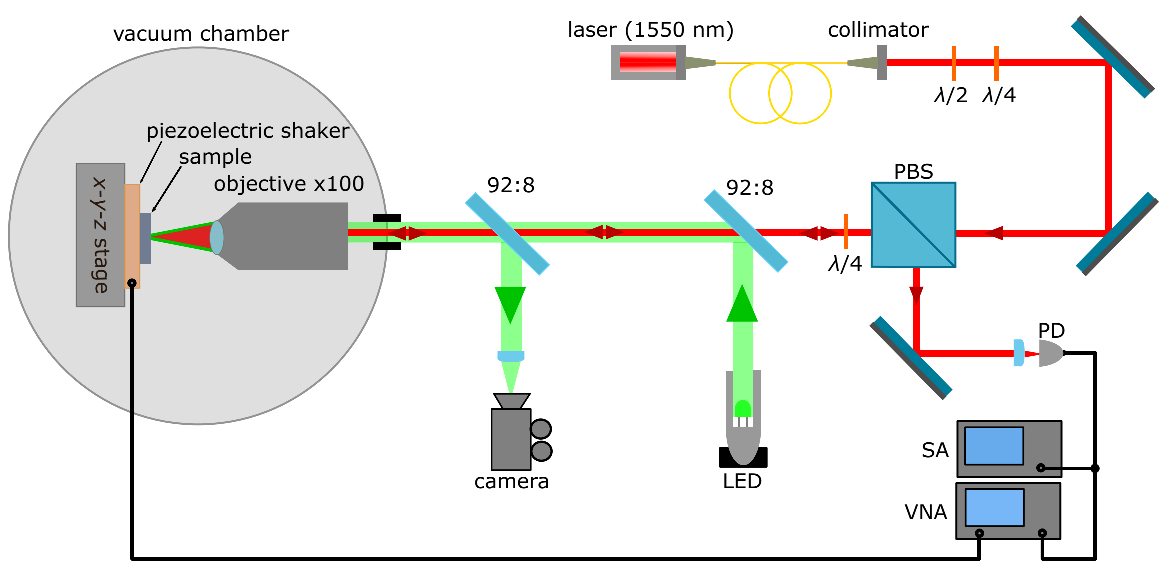

FIG. 6. Optical measurement setup to measure the deflection of the nanomechanical string resonator. LED, light-emitting diode; PBS, polarizing beam splitter; PD, photodetector; SA, spectrum analyzer; VNA, vector network analyzer; $\lambda/2$; half-wave plate; $\lambda/4$; quarter-wave plate.

The electrical signal of the photodetector is measured by a vector network analyzer for frequency-response measurements or with a spectrum analyzer to conduct ringdown measurements. To navigate on the sample and to find the string resonators, an additional light-emitting diode and a camera are coupled to the beam path with weakly reflecting 92:8 mirrors. The sample is moved by attocube positioners. The high-frequency drive is applied by a piezoelectric plate underneath the chip. During the measurement, the focus objective, the sample, and the x-y-z positioner are held in a vacuum with pressure lower than 1×10^{-3} mbar.

An increase of the drive power applied to the piezoelectric shaker increases the amplitude of the mechanical response and thus improves the signal-to-noise ratio. However, too-large drive powers result in a nonlinear mechanical response, which is impractical for the purpose of determining eigenfrequency and linear damping rate. Therefore, for each resonance that we measure, we first determine the drive power at which nonlinear effects become visible and then record the response curve at drive powers well below the onset of nonlinearity. This strategy allows us to obtain the linear frequency-response curve of each resonance with the optimal signal-to-noise ratio.

APPENDIX D: FREQUENCY RESPONSE AND RINGDOWN FIT FUNCTIONS

We use the conventions implied by the equation of motion for the driven damped harmonic oscillator

$$\ddot{x} + \Gamma\dot{x} + {\omega_0}^2 x = A_d \cos(\omega_d t), \tag{D1}$$

with deflection x, damping rate Γ (i.e., energy decay rate), resonance frequency $\omega_0 = 2\pi f_0$, driving frequency ω_d, driving force normalized to effective mass A_d, and time t. The fit functions used for the measured amplitude-response curves and amplitude-ringdown traces are given by

$$A_{\text{response}}(\omega_d) = \frac{\Gamma\omega_0 A_0}{\sqrt{({\omega_0}^2 - {\omega_d}^2)^2 + \Gamma^2{\omega_d}^2}} + A_{\text{noise}}, \tag{D2}$$

$$A_{\text{ringdown}}(t) = A_0 e^{-t\Gamma/2} + A_{\text{noise}}, \tag{D3}$$

with signal amplitude A_0 and experimental noise floor A_{noise}. The parameters A_0, ω_0, Γ, and A_{noise} are free fit parameters. All damping rates and amplitudes mentioned in the main text follow these conventions.

[1] A. Acín, I. Bloch, H. Buhrman, T. Calarco, C. Eichler, J. Eisert, D. Esteve, N. Gisin, S. J. Glaser, F. Jelezko, S. Kuhr, M. Lewenstein, M. F. Riedel, P. O. Schmidt, R. Thew, A. Wallraff, I. Walmsley, and F. K. Wilhelm, The quantum technologies roadmap: A European community view, New J. Phys. **20**, 080201 (2018).

[2] O. Van Deventer, *et al.*, Towards European standards for quantum technologies, EPJ Quantum Technol. **9**, 33 (2022).

[3] G. Kurizki, P. Bertet, Y. Kubo, K. Mølmer, D. Petrosyan, P. Rabl, and J. Schmiedmayer, Quantum technologies with hybrid systems, Proc. Natl. Acad. Sci. USA **112**, 3866 (2015).

[4] H. Wang and I. Lekavicius, Coupling spins to nanomechanical resonators: Toward quantum spin-mechanics, Appl. Phys. Lett. **117**, 230501 (2020).

[5] M. Aspelmeyer, T. J. Kippenberg, and F. Marquardt, Cavity optomechanics, Rev. Mod. Phys. **86**, 1391 (2014).

[6] D. Lee, K. W. Lee, J. V. Cady, P. Ovartchaiyapong, and A. C. B. Jayich, Topical review: Spins and mechanics in diamond, J. Opt. **19**, 033001 (2017).

[7] L. V. H. Rodgers, L. B. Hughes, M. Xie, P. C. Maurer, S. Kolkowitz, A. C. Bleszynski Jayich, and N. P. de Leon, Materials challenges for quantum technologies based on color centers in diamond, MRS Bull. **46**, 623 (2021).

[8] Y. T. Yang, K. L. Ekinci, X. M. H. Huang, L. M. Schiavone, M. L. Roukes, C. A. Zorman, and M. Mehregany, Monocrystalline silicon carbide nanoelectromechanical systems, Appl. Phys. Lett. **78**, 162 (2001).

[9] C. Zorman and M. Mehregany, in *Proceedings of IEEE Sensors* (IEEE, Orlando, FL, USA, 2002), Vol. 2, p. 1109.

[10] Y. T. Yang, C. Callegari, X. L. Feng, K. L. Ekinci, and M. L. Roukes, Zeptogram-scale nanomechanical mass sensing, Nano Lett. **6**, 583 (2006).

[11] M. Li, H. X. Tang, and M. L. Roukes, Ultra-sensitive NEMS-based cantilevers for sensing, scanned probe and very high-frequency applications, Nat. Nanotechnol. **2**, 114 (2007).

[12] A. R. Kermany, G. Brawley, N. Mishra, E. Sheridan, W. P. Bowen, and F. Iacopi, Microresonators with Q-factors over a million from highly stressed epitaxial silicon carbide on silicon, Appl. Phys. Lett. **104**, 081901 (2014).

[13] E. Romero, V. M. Valenzuela, A. R. Kermany, L. Sementilli, F. Iacopi, and W. P. Bowen, Engineering the dissipation of crystalline micromechanical resonators, Phys. Rev. Appl. **13**, 044007 (2020).

[14] Y. S. Klaß, J. Doster, M. Bückle, R. Braive, and E. M. Weig, Determining Young's modulus via the eigenmode spectrum of a nanomechanical string resonator, Appl. Phys. Lett. **121**, 083501 (2022).

[15] L. Sementilli, D. M. Lukin, H. Lee, E. Romero, J. Vučković, and W. P. Bowen, Ultralow dissipation nanomechanical devices from monocrystalline silicon carbide, ArXiv:2404.13893.

[16] H. Kraus, V. A. Soltamov, D. Riedel, S. Väth, F. Fuchs, A. Sperlich, P. G. Baranov, V. Dyakonov, and G. V. Astakhov, Room-temperature quantum microwave emitters based on spin defects in silicon carbide, Nat. Phys. **10**, 157 (2014).

[17] R. Nagy, M. Niethammer, M. Widmann, Y.-C. Chen, P. Udvarhelyi, C. Bonato, J. U. Hassan, R. Karhu, I. G. Ivanov, N. T. Son, J. R. Maze, T. Ohshima, O. O. Soykal, A. Gali, S.-Y. Lee, F. Kaiser, and J. Wrachtrup, High-fidelity spin and optical control of single silicon-vacancy centres in silicon carbide, Nat. Commun. **10**, 1954 (2019).

[18] A. L. Falk, B. B. Buckley, G. Calusine, W. F. Koehl, V. V. Dobrovitski, A. Politi, C. A. Zorman, P. X.-L. Feng, and D. D. Awschalom, Polytype control of spin qubits in silicon carbide, Nat. Commun. **4**, 1819 (2013).

[19] H. Kraus, D. Simin, C. Kasper, Y. Suda, S. Kawabata, W. Kada, T. Honda, Y. Hijikata, T. Ohshima, V. Dyakonov, and G. V. Astakhov, Three-dimensional proton beam writing of optically active coherent vacancy spins in silicon carbide, Nano Lett. **17**, 2865 (2017).

[20] Z.-X. He, Q. Li, X.-L. Wen, J.-Y. Zhou, W.-X. Lin, Z.-H. Hao, J.-S. Xu, C.-F. Li, and G.-C. Guo, Maskless generation of single silicon vacancy arrays in silicon carbide by a focused He^+ ion beam, ACS Photonics **10**, 2234 (2023).

[21] A. V. Poshakinskiy and G. V. Astakhov, Optically detected spin-mechanical resonance in silicon carbide membranes, Phys. Rev. B **100**, 094104 (2019).

[22] J. Chen, A. J. Steckl, and M. J. Loboda, Molecular beam epitaxy growth of SiC on Si(111) from silacyclobutane, J. Vac. Sci. Technol. B **16**, 1305 (1998).

[23] G. I. González and P. R. Saulson, Brownian motion of a mass suspended by an anelastic wire, J. Acoust. Soc. Am. **96**, 207 (1994).

[24] Q. P. Unterreithmeier, T. Faust, and J. P. Kotthaus, Damping of nanomechanical resonators, Phys. Rev. Lett. **105**, 027205 (2010).

[25] P.-L. Yu, T. P. Purdy, and C. A. Regal, Control of material damping in high-Q membrane microresonators, Phys. Rev. Lett. **108**, 083603 (2012).

[26] S. S. Verbridge, J. M. Parpia, R. B. Reichenbach, L. M. Bellan, and H. G. Craighead, High quality factor resonance at room temperature with nanostrings under high tensile stress, J. Appl. Phys. **99**, 124304 (2006).

[27] G. D. Cole, P.-L. Yu, C. Gärtner, K. Siquans, R. Moghadas Nia, J. Schmöle, J. Hoelscher-Obermaier, T. P. Purdy, W. Wieczorek, C. A. Regal, and M. Aspelmeyer, Tensile-strained $In_xGa_{1-x}P$ membranes for cavity optomechanics, Appl. Phys. Lett. **104**, 201908 (2014).

[28] A. Beccari, D. A. Visani, S. A. Fedorov, M. J. Bereyhi, V. Boureau, N. J. Engelsen, and T. J. Kippenberg, Strained crystalline nanomechanical resonators with quality factors above 10 billion, Nat. Phys. **18**, 436 (2022).

[29] A. Ciers, A. Jung, J. Ciers, L. Radit Nindito, H. Pfeifer, A. Dadgar, A. Strittmatter, and W. Wieczorek, Nanomechanical crystalline AlN resonators with high quality factors for quantum optoelectromechanics, ArXiv:2402.12196.

[30] M. Xu, D. Shin, P. M. Sberna, R. van der Kolk, A. Cupertino, M. A. Bessa, and R. A. Norte, High-strength amorphous silicon carbide for nanomechanics, Adv. Mater. **36**, 2306513 (2024).

[31] F. I. Allen, A review of defect engineering, ion implantation, and nanofabrication using the helium ion microscope, Beilstein J. Nanotechnol. **12**, 633 (2021).

[32] G. Hlawacek and A. Gölzhäuser, eds., *Helium Ion Microscopy*, NanoScience and Technology (Springer International Publishing, Cham, 2016).

[33] J. Xi, P. Zhang, C. He, H. Zang, D. Guo, and T. Li, The role of point defects in the swelling and elastic modulus of irradiated cubic silicon carbide, Nucl. Instrum. Methods Phys. Res. B **356–357**, 62 (2015).

[34] S. Nogami, A. Hasegawa, L. L. Snead, R. H. Jones, and K. Abe, Effect of He pre-implantation and neutron irradiation on mechanical properties of SiC/SiC composite, J. Nucl. Mater. **329–333**, 577 (2004), Proceedings of the 11th International Conference on Fusion Reactor Materials (ICFRM-11).

[35] Y. Katoh, H. Kishimoto, and A. Kohyama, The influences of irradiation temperature and helium production on the dimensional stability of silicon carbide, J. Nucl. Mater. **307–311**, 1221 (2002).

[36] W. Jiang, W. Weber, S. Thevuthasan, and D. McCready, Accumulation and recovery of irradiation damage in He^+ implanted α-SiC, J. Nucl. Mater. **257**, 295 (1998).

[37] H. K. Henisch and R. Roy, *Silicon Carbide 1968—Proceedings of the International Conference on Silicon Carbide* (Elsevier, Elmsford, NY, 2013).

[38] G. L. Harris, *Properties of Silicon Carbide* (IEE, London, UK, 1995), Vol. 13.

[39] M. Bückle, Y. S. Klaß, F. B. Nägele, R. Braive, and E. M. Weig, Universal length dependence of tensile stress in nanomechanical string resonators, Phys. Rev. Appl. **15**, 034063 (2021).

[40] M. G. Grimaldi, L. Calcagno, P. Musumeci, N. Frangis, and J. Van Landuyt, Amorphization and defect recombination in ion implanted silicon carbide, J. Appl. Phys. **81**, 7181 (1997).

[41] K. L. Ekinci, Electromechanical transducers at the nanoscale: Actuation and sensing of motion in nanoelectromechanical systems (NEMS), Small **1**, 786 (2005).

[42] S. Schmid, L. G. Villanueva, and M. L. Roukes, *Fundamentals of Nanomechanical Resonators* (Springer International Publishing, 2016).

[43] J. F. Barbot, M. F. Beaufort, and V. Audurier, Effects of helium implantation on the mechanical properties of 4H-SiC, Materials Science Forum **645–648**, 721 (2010).

[44] M. Hollenbach, C. Kasper, D. Erb, L. Bischoff, G. Hlawacek, H. Kraus, W. Kada, T. Ohshima, M. Helm, S. Facsko, V. Dyakonov, and G. V. Astakhov, Ultralong-term high-density data storage with atomic defects in SiC, Adv. Funct. Mater. **34**, 2313413 (2024).

[45] C. Babin, *et al.*, Fabrication and nanophotonic waveguide integration of silicon carbide colour centres with preserved spin-optical coherence, Nat. Mater. **21**, 67 (2022).

[46] https://doi.org/10.14278/rodare.3024